In Vivo Nanoparticle Imaging

Deutsche Ausgabe: DOI: 10.1002/ange.201505525
Internationale Ausgabe: DOI: 10.1002/anie.201505525

Heat-Induced Radiolabeling of Nanoparticles for Monocyte Tracking by PET

*Marc D. Normandin, Hushan Yuan, Moses Q. Wilks, Howard H. Chen, Joseph M. Kinsella, Hoonsung Cho, Nicolas J. Guehl, Nader Absi-Halabi, Seyed Mohammadreza Hosseini, Georges El Fakhri, David E. Sosnovik, and Lee Josephson**

Abstract: *Heat-induced radiolabeling (HIR) yielded ^{89}Zr-Feraheme (FH) nanoparticles (NPs) that were used to determine NP pharmacokinetics (PK) by positron emission tomography (PET). Standard uptake values indicated a fast hepatic uptake that corresponded to blood clearance, and a second, slow uptake process by lymph nodes and spleen. By cytometry, NPs were internalized by circulating monocytes and monocytes in vitro. Using an IV injection of HIR ^{89}Zr-FH (rather than in vitro cell labeling), PET/PK provided a view of monocyte trafficking, a key component of the immune response.*

We continue the development of the heat-induced radiolabeling (HIR) technique,[1] which uses Feraheme (FH) NPs, approved for treating iron anemia in the US and EU by bolus injection of 500 mg Fe, for radiolabeling. HIR uses heat rather than covalent modification to tightly bond ^{89}Zr to FH NPs and, as shown herein, does so without modifying the physical and biological properties of the drug (except for the binding of trace amounts of ^{89}Zr to a far larger amount of iron). FH has been used off-label as a MRI contrast agent, to determine macrophage activity in clinical neuroinflammation,[2] CNS neoplasms,[3] type I diabetes,[4] and myocardial infarction.[5] FH has also been used to determine the metastatic status of normal-sized lymph nodes (LNs).[6]

Our goals were (1) using physical and biological techniques, to demonstrate the equivalence of the FH drug and HIR-generated ^{89}Zr-FH; and (2) using PET-derived standard uptake values (SUVs), to model NP pharmacokinetics (PK) in normal mice. Based on the propensity of a fluorescent FH NP to be internalized by monocytes, we propose that the trafficking of ^{89}Zr-FH-loaded monocytes accounts for the slow uptake of ^{89}Zr-FH by the spleen and lymph nodes. Therefore, HIR-generated ^{89}Zr-FH and PET/PK modelling was used to image monocyte trafficking, the source of macrophages for normal lymph nodes and inflammatory pathologies. Previous methods of cell tracking employ an in vitro cell labeling step that can modify the function of cells when tracked by imaging.[7]

For pre-clinical PET imaging research, the HIR method offers the use of a widely available NP (FH) and radiolabels it with a simple heating procedure. In the clinical arena, HIR-generated FH and PET has potential advantages over the FH/MRI of iron dose reduction and the use of standard uptake values (SUVs) to obtain a quantitative PK analysis. These goals further the long-term goal of using HIR-generated NPs to image monocyte trafficking in clinical settings, permitting an argument for minimal toxicology studies and assisting in planning additional pre-clinical or clinical PK studies.

The HIR procedure shown in Figure 1a consists of heating a radioactive metal ion (^{89}Zr^{4+}) with FH NPs (120 °C, 2 h, "Loading Step"), followed by incubation with

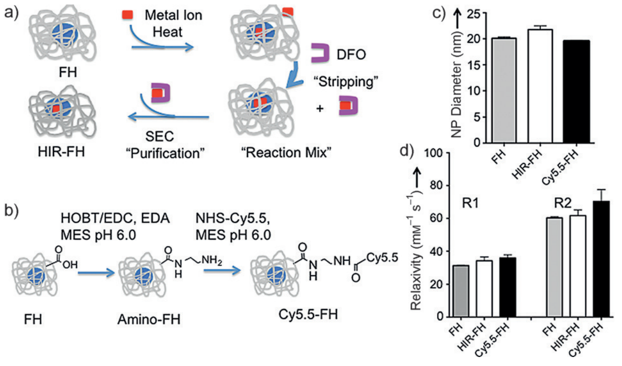

Figure 1. Nanoparticle synthesis. a) HIR steps are heat induced "Loading", DFO "Stripping", and size exclusion "Purification". FH consists of a superparamagnetic iron oxide core (blue ball) and coating of carboxymethyldextran (CMD, gray). b) Synthesis of Cy5.5-FH. The carboxyl groups of FH carboxymethyldextran are reacted with ethylene diamine (EDA) and the resulting amino-FH is reacted with an NHS ester of Cy5.5. c) Sizes of the FH, HIR-FH, and Cy5.5-FH. d) Relaxivities of the FH, HIR-FH, and Cy5.5-FH NPs.

---

[*] Prof. M. D. Normandin, Dr. H. Yuan, Dr. M. Q. Wilks, N. J. Guehl, N. Absi-Halabi, S. M. Hosseini, Prof. G. El Fakhri, Prof. L. Josephson
Center for Advanced Medical Imaging Sciences,
Department of Radiology,
Massachusetts General Hospital
55 Fruit Street, Boston, MA 02114 (USA)
E-mail: ljosephson@mgh.harvard.edu

Prof. J. M. Kinsella
McGill University, Department of Bioengineering
817 Sherbrook Street, Montreal, Quebec H3A 0C3 (Canada)

Dr. H. Cho
School of Materials Science and Engineering,
Chonnam National University
Gwangju, 500-75 (South Korea)

Dr. H. H. Chen, Prof. D. E. Sosnovik, Prof. L. Josephson
Martinos Center for Biomedical Imaging,
Massachusetts General Hospital
149 13th St., Charlestown, MA 02129 (USA)

Supporting information for this article (experimental methods and additional data comprising TLC of HIR reaction mixes, TLC of HIR NPs stability, relativities of FH in mouse serum, and sagittal PET/CT images showing both spleen and liver) is available on the WWW under http://dx.doi.org/10.1002/anie.201505525.

deferoxamine (DFO) to remove loosely bound cations ("Stripping"), followed by size exclusion chromatography (SEC) to separate DFO:metal complexes for the ^{89}Zr-FH NPs ("Purification"). Thus, DFO is used to strip away loosely bound ions and does not participate in the bonding of the radiometal to the NP. The HIR method can employ three cations used in imaging: ^{89}Zr, ^{111}In, or ^{64}Cu, giving radiolabeled NPs of high purity and stability (Supporting Information, Figures S1, S2).

To identify the cells internalizing FH by flow cytometry (Figure 4), we synthesized a fluorescent FH (Cy5.5-FH, Figure 1 b) and compared Cy5.5-FH with FH (Figure 1 c, d).

By light scattering, FH, HIR FH, and Cy5.5-FH were not significantly different ($p > 0.05$) with diameters of 20.1 ± 0.5, 21.8 ± 1.2 nm, and 19.5 ± 0.4 nm, respectively (Figure 1 c). Values were consistent with the manufacturer's range of 17 to 31 nm (Package Insert). Relaxivities (Figure 1 d) were also not significantly different. The PK of ^{89}Zr-FH and FH were also compared (Figure 2).

To determine the PK of ^{89}Zr-FH, PET/CT images were taken after injection of normal mice at 30 min, 4 h, 24 h, 72 h, and 144 h post-injection. At 30 min (Figure 2 a), ^{89}Zr-FH was evident in the heart blood pool and carotids. At 4 h, hepatic and splenic uptake was dominant, with the hepatic uptake of ^{89}Zr-FH seen in the coronal image (Figure 2 b) and both hepatic and splenic uptake evident on sagittal images (Supporting Information, Figure S3). At 24 h (Figure 2 c), ^{89}Zr-FH was apparent in the renal, popliteal, and axillary lymph nodes (LNs), with LN uptake further increasing over the next six days (Figure 2 d, 7 day image).

Standard uptake values (SUVs) for the liver, spleen, and popliteal and axillary nodes were similar in all four mice, so the means and standard deviations as a function of time after injection are shown in Figure 2 e. (Mouse to mouse variation is discussed below.) ^{89}Zr-FH uptake by popliteal and axillary LNs fit a single exponential, but liver and spleen required a biexponential with fast and slow uptake phases.

To compare the PET-derived PK with blood levels of ^{89}Zr-FH, blood samples were analyzed for radioactivity as shown in Figure 2 f. Data fit a single exponential with a half-life of 1.02 h (Table 1). The blood half-life of the FH NP radiolabeling precursor was also obtained using blood spin–spin relaxation rates (1/T2) as a measure of FH blood concentration, a procedure used to obtain half-lives clinically.[8] The similar blood half-lives for ^{89}Zr-FH ($t_{1/2} = 1.00$ h) and FH ($t_{1/2} = 1.02$ h), together with the lack of change in NP size and relaxivity produced by the HIR procedure (Figure 1 c, d), indicate that the HIR does not change the FH NP, save for the addition of trace amounts of Zr. (The ratio of radiometal to nonradioactive iron is discussed below.) A summary of the half-lives obtained from PET (Figure 2 e) and blood clearance (Figure 2 f) is given in Table 1.

To account for the fast and slow uptake of ^{89}Zr-FH, we propose that the fast ^{89}Zr-FH NP uptake process of liver and

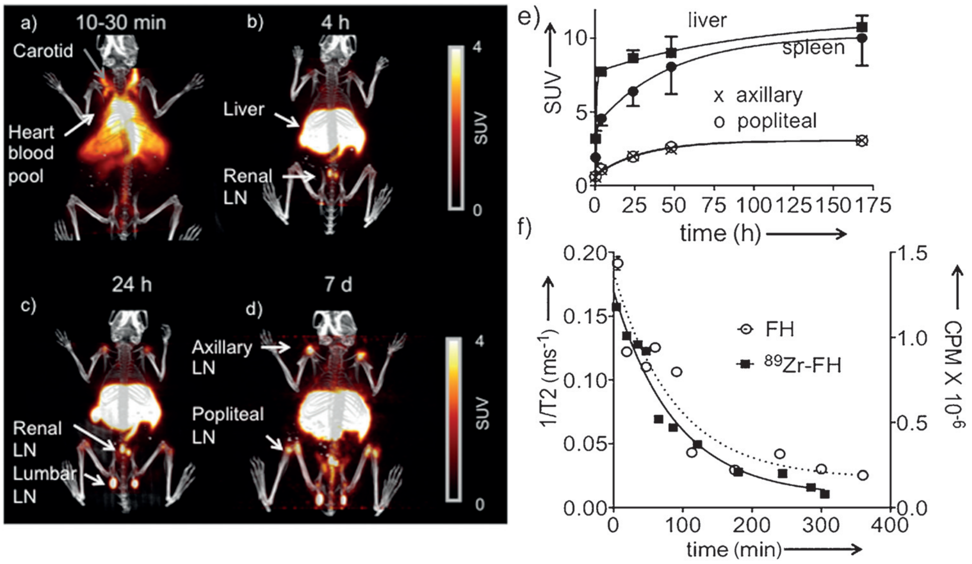

Figure 2. PET pharmacokinetics. a) A representative maximum intensity project (MIP) PET/CT image of a mouse at 30 min after injection, with ^{89}Zr-FH in heart blood pool and carotid arteries. b) A 4 h hepatic phase image where ^{89}Zr-FH is predominately in the liver, with limited uptake in the renal node. With 24 h (c) and 7 d (d) images, nodal radioactivity has increased further. e) Time-dependent SUVs for organs shown as means and standard deviations, $n = 4$. Nodal SUVs fit to a mono-exponential equation, while liver and spleen fit a biexponential with constants given in Table 1. f) Blood radioactivity (following an injection of ^{89}Zr-FH) and blood 1/T2 relaxation rates (following an injection of FH) as a function of time after injection.

Table 1: Kinetic constants (K_{fast}, K_{slow}) and corresponding half-lives ($t_{1/2,fast}$, $t_{1/2,slow}$) for ^{89}Zr-FH pharmacokinetics.

	K_{fast} [h^{-1}]	$t_{1/2,fast}$ [h]	K_{slow} [h^{-1}]	$t_{1/2,slow}$ [h]	Figure
clearance by T2[a]	0.69	1.00 *0.7 to 1.67*	–[b]		2 f
clearance by ^{89}Zr[a]	0.68	1.02 *0.70 to 2.63*	–[b]		2 f
axillary LN[a]	–[b]		0.033	21.2 *12.3 to 77*	2 e
popliteal LN[a]	–[b]		0.034	20.2 *12.2 to 57.8*	2 e
liver[a]	0.55	1.27 *1.03 to 1.64*	$5. \times 10^{-5}$	1.16×10^{4} *47.5 to ∞*	2 e
spleen[a]	0.56	1.24 *0.074 to 3.73*	0.0191	36.3 *26.1 to 59.3*	2 e

[a] 95 % confidence limits are given in italics for half-lives. [b] Single-exponential function.

spleen results from a direct NP phagocytosis while the slow uptake process results from the uptake of ^{89}Zr-FH by blood borne monocytes, followed by slow trafficking to the lymph nodes (LNs) and spleen (Figure 3).

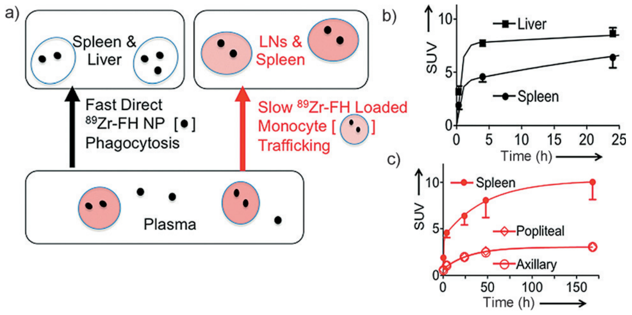

Figure 3. A model for the fast and slow uptake of ^{89}Zr-FH seen with PET SUV analysis. a) Fast uptake by liver and spleen results from the direct ^{89}Zr-FH phagocytosis from the plasma. The slow uptake process results from the trafficking of ^{89}Zr-FH loaded monocytes. b) SUVs for fast uptake of liver and spleen from Figure 2e. c) Slow uptake by spleen, and popliteal and axillary nodes from Figure 2e.

A fast clearance process was evident from blood-derived half-lives of 1.02 h and 1.00 h, for ^{89}Zr-FH and FH, respectively (Figure 2f). For liver and spleen, the biexponential fit of SUVs versus time (Figure 2e) yielded fast uptake half-lives of 1.27 h and 1.24 h respectively, with 60.7 % ID and 2.16 % of injected dose found the liver and spleen, respectively, at 24 h. Thus the fast uptake processes of ^{89}Zr-FH seen with PET corresponded to the clearance of ^{89}Zr-FH from blood and resulted from NP phagocytosis by resident splenic and hepatic macrophages.

A second, slow uptake process was evident from the accumulation of ^{89}Zr in axillary and popliteal lymph nodes (LNs) that fit a single exponential function with half-lives of 21.2 h and 20.2 h, respectively. Two distinct uptake processes are indicated because the lower-bound 95 % confidence limits for the slow process were 12.2 h and 12.3 h, far above the upper bound 95 % limit for clearance of ^{89}Zr-FH from blood (2.63 h). The slow uptake process for the spleen ($t_{1/2} = 36.3$ h) did not differ significantly from the slow uptake process of popliteal and axillary lymph nodes.

We propose the model of Figure 3, where the post-injection fast uptake process reflects phagocytosis by tissue macrophages (for example, hepatic Kupffer cells) while the slow uptake process results from a fast internalization by blood monocytes, followed by the slow trafficking of ^{89}Zr-loaded monocytes. Support for this view is provided by similar half-lives of our slow uptake processes (ca. 20–40 h) and half-lives of mouse blood monocytes (ca. 24–48 h) by other techniques, and by monocyte biology, where blood monocytes traffic into LN dendritic cells and tissue macrophages (with replacement of circulating monocytes by the bone marrow).[9]

To obtain direct support for our model, we sought to detect FH in circulating monocytes after the injection of a fluorescent FH (Cy5.5-FH; Figure 1b). We then examined its presence in monocytes by dual-wavelength flow cytometry (Figure 4a,b), where a fluorescein (FITC)-labeled anti-CD11b was used to identify monocytes (x-axis) and a Cy5.5-FH was used to identify cells internalizing FH (y-axis). For in vivo monocyte labeling, mice were injected with either PBS (-Cy5.5-FH) or Cy5.5-FH (+Cy5.5-FH) and buffy coats prepared and analyzed (Figure 4a). Cy5.5 fluorescence was seen in quadrant iii (Figure 4a, CD11b positive cells), but not in quadrant iv (CD11b negative cells), indicating circulating monocytes were the only cells bearing Cy5.5-FH. A similar result was obtained with ex vivo labeling, when PBS or Cy5.5-FH was added to heparinized mouse blood (Figure 4b). However, with in vivo loading, some 4.8 ± 4.4 % of monocytes were Cy5.5-FH positive, compared to 31.9 ± 1.9 % positive for ex vivo loading (Figure 4c). The higher fraction of Cy5.5-FH bearing monocytes achieved with in vitro labeling is expected from the ability of that protocol to maintain a constant, high NP concentration (3 h, 60 µg Fe/mL) and from the closed nature of the system (a lack of monocytes entering and leaving the pool being labeled).

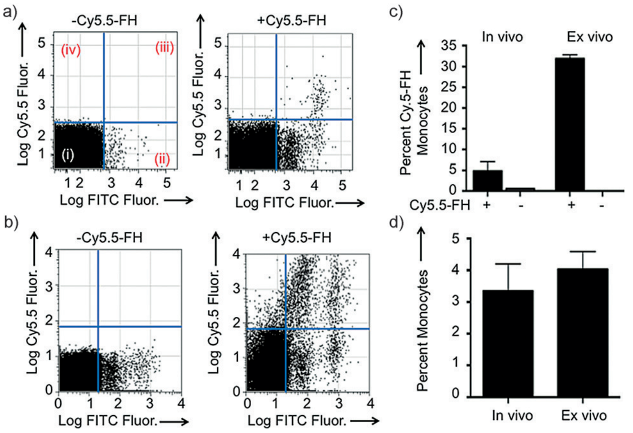

Figure 4. Flow cytometry for Cy5.5-FH uptake of CD11b expressing monocytes in vivo (injection) and ex vivo (heparinized mouse blood). a) Scattergrams for mice injected with PBS (-Cy5.5-FH) or Cy5.5-FH (+Cy5.5-FH) for white cell buffy coats are shown. Scattergrams (e.g. Figure 4a) have four quadrants: i) CD11b-negative (non-monocytes), Cy5.5-FH-negative; ii) CD11b-positive (monocytes), Cy5.5-FH-negative; iii) CD11b-positive, Cy5.5-FH-positive; iv) CD11b-negative, Cy5.5-FH-positive. Cells from a PBS-injected control mouse (-Cy5.5-FH) had no Cy5.5 fluorescence. Two populations of CD11b cells are seen in quadrant (ii). b) Ex vivo monocyte labeling with Cy5.5-FH. c) Fraction of Cy5.5-FH-positive monocytes (iii/(ii + iii)) from in vivo labeling and ex vivo labeling. Results are mean ± 1 SD, $n = 4$. d) Monocyte fraction of total white cells, that is (ii + iii)/total cells).

The percent of total white cells that were monocytes (Figure 4d) was consistent with reports[10] and not significantly different (in vivo: 3.3 ± 1.7 % vs. ex vivo: 4.0 ± 1.1 %, $p > 0.05$). Thus Cy5.5-FH was internalized by CD11b positive monocytes, after injection or in heparinized blood, consistent with the proposal that the trafficking of ^{89}Zr-FH-loaded monocytes yields the slowly increasing SUVs of spleen and LNs.

In contrast to the uniform SUVs for ^{89}Zr-FH uptake by liver, spleen, and axillary and popliteal LNs (Figure 2), uptake by renal and lumbar LNs showed high inter-animal variability (Figure 5a and b). Variable SUVs were seen over the four mice studied and at all times after injection (Figure 5c,d). Seven day SUVs for lumbar LNs ranged from 28 (Figure 5b and c) to 4 (Figure 5a and c). Seven-day SUVs for renal LNs ranged from 16 (Figure 5b,d) to undetectable (Figure 5a,d).

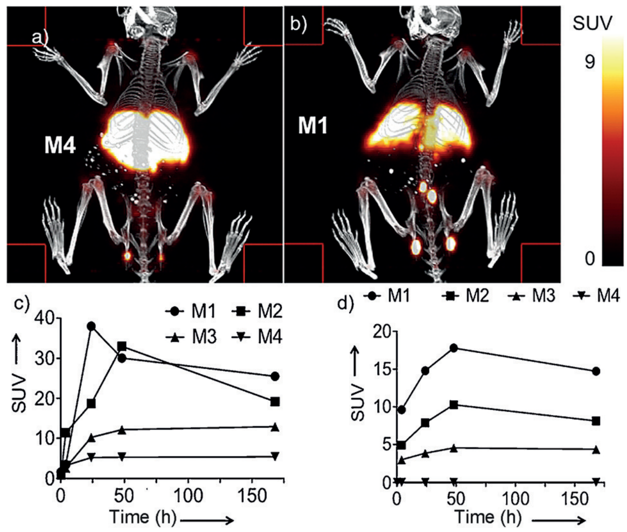

Figure 5. Inter-animal variability in ^{89}Zr-FH uptake in renal and lumbar lymph nodes. MIP PET images for renal and lumbar nodes are shown for mouse 4 (a) and mouse 1 (b) at 7 d post-injection. The time dependence of lumbar and renal lymph node SUVs are shown in (c) and (d), respectively.

The variable SUVs for renal and lumbar LNs may reflect variable LN anatomy[11] or subclinical, individual immune responses to the environment.

Our HIR technique exploits several features of FH. FH has extremely high temperature stability, which is evident from the use of the terminal sterilization step used in its manufacture. The extraordinary heat stability of iron oxides coated with carboxyl alkyl polysaccharides was first noted by Maruno[12] and then by Groman,[13] leading to the development of FH. Second, HIR exploits the pH-dependent stability of FH to chelators. At the neutral pH that HIR employs for "Stripping", DFO binds ^{89}Zr^{4+} without NP dissolution, evident by the lack of change of FH size or relaxivity (Figure 1c). On the other hand, in the mild acid of the phagolysosome, FH is digested and the iron joins normal iron pools, thereby relieving anemia. HIR also exploits the ability of the macrophage/phagocytes to clear large amounts of injected NPs, with our mice receiving injections 5 mg Fe kg^{-1}.

HIR employs a high molar ratio of NP iron to radiometal, with 1 mg of FH iron (17.9 μmoles Fe) and 1 mCi of ^{89}Zr at 4000 mCi/μmole (see the Supporting Information). ^{89}Zr binds to an extremely small number of high affinity sites on the NP. With 5874 Fe atoms per NP (manufacturer's insert), there is less than one mole of zirconium per mole of NP. Magnetic NPs of Molday,[14] which use a dextran coating, can be radiolabeled by HIR, suggesting the carboxyl groups of the FH CMD coating are not involved in radiometal binding.[1]

There was no elimination of ^{89}Zr during our one-week observation period. Consistent with this, radioactivity in the intestine, kidney, or bladder was not seen with PET. Furthermore, analyses of decay corrected PET data summed over the entire imaging field of view indicated that radioactivity at 7 d was 92 ± 2% of that at 24 h. Finally, no radioactivity was detected in the animal waste or bedding. Once injected, FH is too large for renal elimination and is phagocytosed. The iron joins normal body iron stores (alleviating anemia) and the highly charged ^{89}Zr^{4+} cation is tenuously retained, likely by binding to negatively charged biomolecules.

The most common method of radiolabeling magnetic NPs is by the covalent attachment of chelates.[15] However, surface chelates can be "poisoned" by leachable metal ions, if storage of chelate-bearing NPs prior to radiolabeling is attempted. NPs can also be radiolabeled by surface adsorption[16] or by incorporation of a radiometal into the NP during synthesis.[17] However, adsorption may be reversible in biological media and incorporation during synthesis requires short synthetic procedures relative to the radioisotopic half-life. The HIR procedure employs a two-hour high-temperature incubation, followed by short stripping and purification steps, with a total time of about 2.5 h. Radioisotopes with half-lives like ^{64}Cu (half-life = 12.7 h), ^{111}In (half-life = 67.3 h) and ^{89}Zr (half-life = 78.4 h) have been used (Supporting Information, Figure S1).

Using HIR NPs and PET-derived PK, we describe for the first time fast and slow NP uptake processes, with the slow process resulting from the trafficking of NP-loaded monocytes. We also describe inter-animal variability of NP LN uptake in normal mice. The simplicity of the HIR procedure and availability of FH NPs may speed the adaptation of HIR-generated NPs in pre-clinical or clinical imaging research and lead to further insights in the metabolism of nanomaterials.

Acknowledgements

This work was supported by R01 NIH grants EB011996 (L.J.), EB009691 (L.J.), MH100350 (M.D.N.), CA165221 (G.E.F.), HL110241 (G.E.F.), HL112831 (D.E.S.) and NIH K99L121152 (H.H.C.), and T32EB013180 (G.E.F.). We thank K. Takahashi for assistance with animal handling procedures. The authors declare they have no conflict of interest.

Keywords: heat-induced radiolabeling · imaging · monocyte trafficking · nanoparticles · positron emission tomography · pharmacokinetics

How to cite: *Angew. Chem. Int. Ed.* **2015**, *54*, 13002–13006
Angew. Chem. **2015**, *127*, 13194–13198

---

[1] E. Boros, A. M. Bowen, L. Josephson, N. Vasdev, J. P. Holland, *Chem. Sci.* **2014**, *6*, 225-236.

[2] M. Nasseri, S. Gahramanov, J. P. Netto, R. Fu, L. L. Muldoon, C. Varallyay, B. E. Hamilton, E. A. Neuwelt, *Neuro-oncology* **2014**, *16*, 1146-1154.

[3] C. G. Varallyay, E. Nesbit, R. Fu, S. Gahramanov, B. Moloney, E. Earl, L. L. Muldoon, X. Li, W. D. Rooney, E. A. Neuwelt, *J. Cereb. Blood Flow Metab.* **2013**, *33*, 780 – 786.

[4] J. L. Gaglia, A. R. Guimaraes, M. Harisinghani, S. E. Turvey, R. Jackson, C. Benoist, D. Mathis, R. Weissleder, *J. Clin. Invest.* **2011**, *121*, 442 – 445.

[5] P. Storey, R. P. Lim, H. Chandarana, A. B. Rosenkrantz, D. Kim, D. R. Stoffel, V. S. Lee, *Invest. Radiol.* **2012**, *47*, 717 – 724.

[6] a) M. Harisinghani, R. W. Ross, A. R. Guimaraes, R. Weissleder, *Neoplasia* **2007**, *9*, 1160 – 1165; b) S. M. MacDonald, M. G. Harisinghani, A. Katkar, B. Napolitano, J. Wolfgang, A. G. Taghian, *Int. J. Radiat. Oncol. Biol. Phys.* **2010**, *77*, 1098 – 1104.

[7] a) N. Sato, H. Wu, K. O. Asiedu, L. P. Szajek, G. L. Griffiths, P. L. Choyke, *Radiology* **2015**, *275*, 490 – 500; b) C. Van De Wiele, M. Sathekge, A. Maes, *The quarterly journal of nuclear medicine and molecular imaging* **2014**, *58*, 269 – 275.

[8] R. Landry, P. M. Jacobs, R. Davis, M. Shenouda, W. K. Bolton, *Am. J. Nephrol.* **2005**, *25*, 400 – 410.

[9] a) A. Mildner, S. Yona, S. Jung, *Adv. Immunol.* **2013**, *120*, 69 – 103; b) S. Yona, S. Jung, *Curr. Opin. Hematol.* **2010**, *17*, 53 – 59.

[10] a) J. A. Nemzek, G. L. Bolgos, B. A. Williams, D. G. Remick, *Inflammation Res.* **2001**, *50*, 523 – 527; b) M. A. Schnell, C. Hardy, M. Hawley, K. J. Propert, J. M. Wilson, *Hum. Gene Ther.* **2002**, *13*, 155 – 161.

[11] a) B. Marniok, J. Mikusek, K. Slusarczyk, M. Ciszek, *Folia Morphol.* **1994**, *53*, 303 – 307; b) W. Van den Broeck, A. Derore, P. Simoens, *J. Immunol. Methods* **2006**, *312*, 12 – 19.

[12] S. Maruno, M. Hasegawa (Meito Sangyo), US Patent 5,204,457, **1993**.

[13] E. V. Groman, K. G. Paul, T. B. Frigo, H. Bengele, J. M. Lewis, US Patent 6,599,498, **2003**.

[14] R. S. Molday, D. MacKenzie, *J. Immunol. Methods* **1982**, *52*, 353 – 367.

[15] a) P. Wunderbaldinger, L. Josephson, C. Bremer, A. Moore, R. Weissleder, *Magn. Reson. Med.* **2002**, *47*, 292 – 297; b) E. J. Keliher, J. Yoo, M. Nahrendorf, J. S. Lewis, B. Marinelli, A. Newton, M. J. Pittet, R. Weissleder, *Bioconjugate Chem.* **2011**, *22*, 2383 – 2389; c) D. L. Thorek, D. Ulmert, N. F. Diop, M. E. Lupu, M. G. Doran, R. Huang, D. S. Abou, S. M. Larson, J. Grimm, *Nat. Commun.* **2014**, *5*, 3097.

[16] F. Chen, P. A. Ellison, C. M. Lewis, H. Hong, Y. Zhang, S. Shi, R. Hernandez, M. E. Meyerand, T. E. Barnhart, W. Cai, *Angew. Chem. Int. Ed.* **2013**, *52*, 13319 – 13323; *Angew. Chem.* **2013**, *125*, 13561 – 13565.

[17] a) B. Freund, U. I. Tromsdorf, O. T. Bruns, M. Heine, A. Giemsa, A. Bartelt, S. C. Salmen, N. Raabe, J. Heeren, H. Ittrich, R. Reimer, H. Hohenberg, U. Schumacher, H. Weller, P. Nielsen, *ACS nano* **2012**, *6*, 7318 – 7325; b) D. Pouliquen, J. J. Le Jeune, R. Perdrisot, A. Ermias, P. Jallet, *Magn. Reson. Imaging* **1991**, *9*, 275 – 283.

Received: June 15, 2015
Revised: July 22, 2015